

# Joint Theoretical/Experimental Highlight on the Formation of Carbides on Ru Nanoparticles during CO Hydrogenation

Received 00th January 20xx,  
Accepted 00th January 20xx

Ionut-Tudor Moraru,<sup>\*a,b</sup> Luis M. Martínez-Prieto,<sup>\*c</sup> Yannick Coppel,<sup>d</sup> Bruno Chaudret,<sup>a</sup> Lucy Cusinato,<sup>a</sup> Iker del Rosal<sup>a</sup> and Romuald Poteau<sup>\*a</sup>

DOI: 10.1039/x0xx00000x

Formation of stable carbides during CO bond dissociation on small ruthenium nanoparticles (RuNPs) is demonstrated, both by means of DFT calculations and by solid state <sup>13</sup>C-NMR techniques. Theoretical calculations of the chemical shifts in several model clusters are employed in order to secure the experimental spectroscopic assignments for the surface ruthenium carbides. Mechanistic DFT investigations, carried out on a realistic Ru<sub>55</sub> nanoparticle model (~1nm) in terms of size, structure and surface composition, reveal that ruthenium carbides are obtained during CO hydrogenation. Calculations also indicate that carbide formation via hydrogen-assisted hydroxymethylidyne (COH) pathways is exothermic, and occurs at reasonable kinetic cost on standard sites of the RuNPs, such as the 4-fold ones on the flat terraces, and not only in steps as previously suggested. Another novel outcome of the DFT mechanistic study consists in the possible formation of  $\mu_6$  ruthenium carbides in the tip-B<sub>5</sub> site, similar examples being known only for molecular ruthenium clusters. Moreover, based on DFT energies, the possible rearrangement of the surface metal atoms around the same tip-site results in a  $\mu$ -Ru atom coordinated to the remaining RuNP moiety, reminiscent of a pseudo-octahedral metal center on the NP surface.

## Introduction

The investigation of transition metal carbides (TMCs) has gained an increased interest during the last decades, owing to their spectacular catalytic and structural properties. Following the seminal paper of Levy and Boudart,<sup>1</sup> the platinum-like activity for TMCs of early d-block elements has been highlighted in several studies.<sup>2,3</sup> The sharp contrast between TMCs and their bare metallic counterparts was related to a tuning of the electronic properties owing to the presence of carbides.<sup>2</sup> As an example, the enhanced stability of tetra-coordinate nickel and cobalt carbides is attributed to local aromaticity induced by the carbide.<sup>4</sup>

TMCs are also active species involved in the production of non-polluting and renewable fuels. Several applications including hydrogen evolution reaction (HER),<sup>5,6</sup> water gas shift (WGS),<sup>2,7</sup> direct alcohol fuel cells (DAFC),<sup>2,8</sup> or biomass conversion,<sup>2,9</sup> are commonly reported for TMC catalysts of molybdenum and wolfram. Other examples of effective TMC catalysts include iron carbides which are active species in the Fischer-Tropsch synthesis (FTS).<sup>10</sup> Regarding FTS, syngas (CO + H<sub>2</sub>) conversion into long-chain hydrocarbons, it is of high interest for its potential application in liquid fuel production with low environmental impact.<sup>11-13</sup> Common catalysts displaying high activities towards liquid alkanes are based on iron,<sup>14-17</sup> cobalt,<sup>18-21</sup> and ruthenium.<sup>22-25</sup> Among these metals, only iron carbides

are effective TMC catalysts for FTS,<sup>10</sup> as bare iron surfaces and nanoparticles (NPs) display poor activities.<sup>15-17,26</sup> Cobalt carbides are less effective in the FTS than their pure metallic analogues as they yield alcohols,<sup>10,27</sup> whereas only metal catalysts are known in the case of ruthenium.<sup>28-32</sup>

Carbide formation during the CO bond cleavage step of ruthenium-catalyzed FTS was theoretically proposed to occur on several ruthenium slab and NP models.<sup>30,31,33-36</sup> On RuNPs, previous computational studies suggest that carbides are obtained only in surface defects, such as the B<sub>5</sub> and B<sub>6</sub> sites of NPs, and that the reaction occurs via direct CO dissociation pathways.<sup>30,33</sup> However, commonly used models imply low CO surface coverage, and with the noticeable exception of Ref. 30, much lower than 1.0 CO per surface mono-layer (1.0 ML CO), thus lacking to reproduce both the steric interactions between co-adsorbed CO molecules and the stabilization of the metal surface Gibbs free energy due to adsorbed surface species. Under FTS conditions, where the CO coverage is much higher<sup>37</sup> (around 1.5 ML CO), several studies indicate that hydrogen-assisted CO dissociation pathways are most likely to occur on both flat terraces,<sup>38-41</sup> and also in defective sites.<sup>31</sup> But possible carbide formation on RuNPs was only suggested as a transient species at step-edges.

To our knowledge, whereas the molecular chemistry of ruthenium carbide complexes is well documented<sup>42</sup> with various examples being reported for small ruthenium clusters, the formation of metallic carbides in mild conditions on pure and well-defined ruthenium NPs has never been firmly established by experimental means. However, thirty years old <sup>13</sup>C-NMR studies proposed the formation of ruthenium carbides on silica-supported and unsupported ruthenium materials using NMR evidence.<sup>43,44</sup>

Previous work<sup>37</sup> by our group on the surface composition of ultra-small RuNPs (~1 nm) suggested on the basis of DFT energies that ruthenium carbides can be stabilized together with the formation of water during the first steps of the FTS process. Formation of such a surface carbide-water intermediate is highly exothermic (-22 kcal mol<sup>-1</sup>), yet a detailed

<sup>a</sup> Université de Toulouse; INSA, UPS, CNRS; LPCNO (IRSAMC), 135 avenue de Rangueil, F-31077 Toulouse, France. E-mail: romuald.poteau@univ-tlse3.fr

<sup>b</sup> Universitatea Babeş-Bolyai, Facultatea de Chimie și Inginerie Chimică, Departamentul de Chimie, str. Kogalniceanu, nr. 1, RO-400084 Cluj-Napoca, Romania. E-mail: ionut.moraru@ubbcluj.ro

<sup>c</sup> Instituto de Tecnología Química (UPV-CSIC), Universitat Politècnica de València, Av. de los Naranjos S/N, 46022, Valencia, Spain. E-mail: luismiguel.martinez@csic.es

<sup>d</sup> CNRS, LCC (Laboratoire de Chimie de Coordination), Université de Toulouse, UPS, INPT, 205 route de Narbonne, BP 44099, F-31077 Toulouse Cedex 4, France

† Electronic Supplementary Information (ESI) available: solid-state <sup>13</sup>C-NMR spectra; DFT-GIAO NMR data; DFT mechanistic investigations; calculated charges, pDOS and pCOHP profiles for carbides and surface molecular complexes. See DOI: 10.1039/x0xx00000x

mechanistic study is required for evaluating the kinetic accessibility of this species. It must also be stressed that due to higher adsorption energies of CO molecules compared to H<sub>2</sub> ones, under FTS conditions (3 bar, CO and H<sub>2</sub> in molar ratios of 1:1) the surface of RuNPs is saturated with COs. According to theoretical calculations,<sup>37,38,40</sup> the optimal surface composition displays *ca.* 1.5 CO/Ru<sub>surface</sub> atom, while hydrides co-adsorption is expected to occur in much lower ratios. Titration reactions with norbornane of RuNPs stabilized by polyvinylpyrrolidone (Ru/PVP) after FTS conditions confirm that this process occurs on CO-saturated RuNPs.<sup>37</sup> However, given that formation of a carbide-water surface species requires a minimum amount of adsorbed hydrides, we further suggest that the adsorption of dihydrogen in small amounts on the ruthenium surface of the RuNPs is most probably due to a thermodynamic driving force which is closely related to the highly exothermic  $\text{CO}^* + 2\text{H}^* \rightarrow \text{C}^* + \text{H}_2\text{O}^*$  transformation.

The joint experimental/theoretical study reported herein aims at bringing fundamental insights into the early steps of the CO hydrogenation catalyzed by RuNPs. On the basis of experimental solid-state NMR techniques and theoretical calculations we highlight for the first time that long-lifetime carbides are systematically formed during CO dissociation on standard sites on the surface of pure and ultra-small RuNPs. Given the potential implication of such carbide species in the Fischer-Tropsch synthesis, a detailed investigation of their formation is needed. In this respect, DFT explorations of carbide formation mechanisms are carried out on realistic models in terms of size, structure and surface coverage achieved during CO hydrogenation conditions. From a mechanistic viewpoint, surface carbides can be formed either through direct CO dissociation or within hydrogen-assisted routes involving hydroxymethylidyne (COH) intermediates. Since at high CO coverage the direct bond cleavage is less probable to occur, according to previous DFT investigations,<sup>31,38,40</sup> the present study addresses the carbide formation issue mainly via the COH pathway. However, direct CO dissociation routes are also assessed on our RuNP model for further comparisons. The DFT mechanistic study is achieved on a 1 nm hexagonal close-packed (hcp) Ru<sub>55</sub> crystalline model, which exhibits a Ru tip reminiscent of B<sub>5</sub> and B<sub>4</sub> sites (*i.e.* the same model that was studied in detail by means of DFT explorations in Ref. 37). The size of the DFT model is close to the actual size of the RuNPs synthesized in the present work (Figure 1). The DFT investigations performed herein also suggest that ruthenium complexes can be formed on the surface of the RuNPs on ad-atoms sites such as the tip Ru atom on our Ru<sub>55</sub> model.

## Results and Discussions

### <sup>13</sup>C-NMR experimental and DFT data

Ru/PVP were synthesized and used as model catalyst for this study due to three reasons: i) ~1 nm clean surface RuNPs (similar to the Ru<sub>55</sub> model employed in the DFT calculations) can be easily obtained by decomposition of Ru(COD)(COT) under dihydrogen pressure in the presence of PVP (Figure 1a).<sup>45</sup> ii) The resulting RuNPs are ideal for solid-state NMR studies because of the absence of magnetic perturbations (knight shift, ferromagnetism or paramagnetism). iii) Ru/PVP NPs have demonstrated to be active catalysts in FTS under relative mild conditions (150 °C and 3 bar of syngas).<sup>46</sup>

Once chosen, the model catalyst was pressurized with 3 bar of syngas (1:1 molar mixture of H<sub>2</sub> and <sup>13</sup>CO) and heated at 150 °C for 24 h (Ru/PVP<sub>ac</sub>). As it could be observed by Transmission Electron Microscopy (TEM) and High Resolution TEM (HRTEM), there were no significant changes in size, distribution and crystalline structure of Ru/PVP NPs before and after catalytic conditions (Figures 1a-b and S1). The Ru/PVP<sub>ac</sub> NPs were analyzed by solid state Magic-Angle Spinning NMR (MAS-NMR) with the aim of observing the presence of surface carbides on the ruthenium surface. Specifically, a <sup>13</sup>C Hahn echo MAS-NMR spectrum was recorded with a spinning rate of 16 kHz in a 3.2 mm diameter rotor during 48 h. A weak and broad resonance is observed at *ca.* 360 ppm (blue, Figure 2). This signal could potentially be a spinning sideband of the CO signal around 200 ppm, a signal of surface carbides or a superposition of both. To discard one of the two possibilities, we used first CPMG protocol with a spinning rate of 16 kHz to increase the signal to noise ratio of the 360 ppm signal (red, Figure 2). A similar signal-to-noise ratio was obtained for an experiment duration three times lower, demonstrating an important gain in sensitivity with the CPMG experiment. Then we ran the same CPMG experiment with a spinning rate of 20 kHz (green, Figure 2). No clear evidence of a significant shift or of an intensity decrease of the 360 ppm signal is observed. This indicates that the signal at 360 ppm is mainly a real isotropic signal and not a spinning side band. Furthermore, a Hahn echo experiment associated with the TOSS protocol was also ran at a spinning rate of 8 kHz in a 4 mm diameter rotor (black, Figure 2). The TOSS protocol is designed to suppress the spinning sideband signals. Again the 360 ppm signal is clearly observed and this experiment definitively confirms that a resonance is observed in the region expected for carbide species. The broadness of

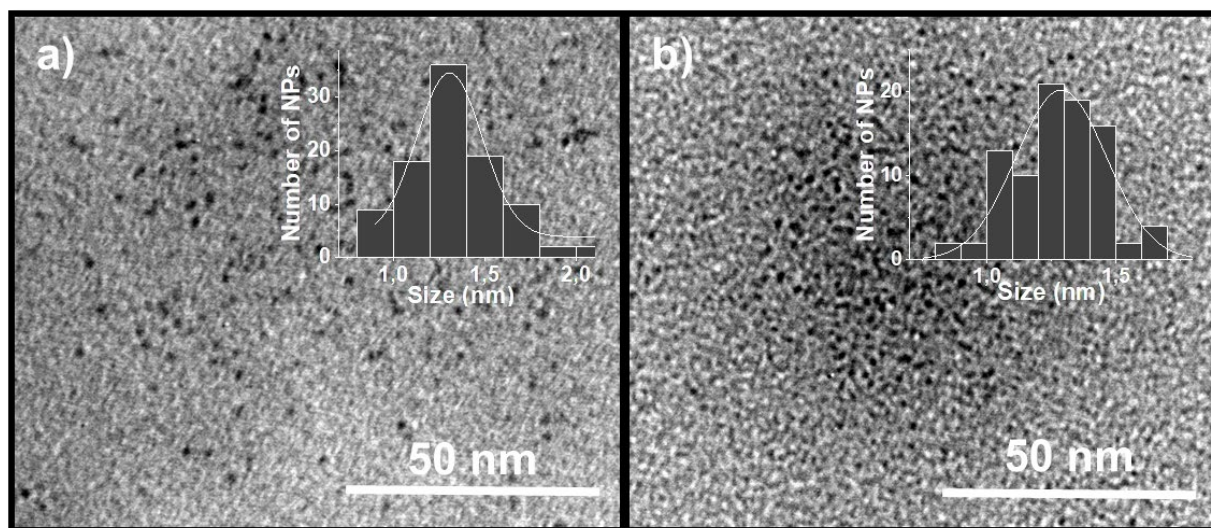


**Figure 1.** (a) TEM micrograph and size histogram of prepared Ru/PVP NPs. Size: 1.3 (0.2) nm. (b) TEM micrograph and size histogram of Ru/PVP NPs after catalytic conditions (Ru/PVP<sub>ac</sub>; 3 bar of syngas, 150°C, 24h). Size: 1.3 (0.4) nm.

this signal is probably related to locally anisotropic diamagnetic susceptibility (heterogeneity). Duncan *et al.* have early reported the presence of a carbide signal near 380 ppm in methanation reactions over a heterogeneous ruthenium catalyst deposited on silica.<sup>43</sup> Yet, molecular anionic ruthenium carbides display a resonance near 450 ppm,<sup>47</sup> but no unambiguous assignment of this *ca.* 400 ppm chemical shift has ever been done.

To evidence the presence of surface carbides on Ru/PVP<sub>ac</sub> that could react with H<sub>2</sub> to form CH<sub>4</sub>, an online hydrogen temperature programmed reduction (H<sub>2</sub>-TPR) study was carried out in a reactor connected to a mass spectrometer (MS). In this experiment, 60 mg of Ru/PVP<sub>ac</sub> was heated from 25 to 400 °C at 5 °C/min under H<sub>2</sub> flow (10 vol % H<sub>2</sub> in Ar; 14

mL·min<sup>-1</sup>). The formation of CH<sub>4</sub> species due to carbide hydrogenation was followed by online MS (see ESI, Figure S4). At 210 °C, the mass signals corresponding to an *m/z* = 16, 15 and 14 clearly increase, confirming the formation of methane. This online experiment is in agreement with the presence of ruthenium surface carbide on Ru/PVP<sub>ac</sub>, but it is likely that some of the methane observed also results from surface CO hydrogenation. However, desorption of CO is observed at higher temperature (see Figure S4), which suggests that the methane produced at low temperature originates in the surface carbides.

Taking advantage of the local character of chemical shieldings, we have developed and successfully applied a computational strategy for computing <sup>1</sup>H, <sup>13</sup>C, <sup>15</sup>N and <sup>19</sup>F chemical shifts<sup>48–51</sup> on model ruthenium carbonyl clusters which replicate specific adsorption sites of RuNPs. Such theoretical chemical shifts turned out to accurately reproduce the experimental NMR spectra of RuNPs. The same computational strategy is employed herein on model [Ru<sub>4</sub>], [Ru<sub>5</sub>] and [Ru<sub>6</sub>] carbonyl clusters for assigning the signals of the experimental <sup>13</sup>C-NMR spectra. Further details on the accuracy of <sup>13</sup>C chemical shift calculations for carbon atoms enclosed in transition metal clusters are available in the ESI (see section 2a). Concerning the [Ru<sub>5</sub>] model cluster, its metal core exhibits a square pyramid configuration in order to replicate the four-fold sites observed, among others, on the (101) crystallographic planes displayed by hexagonal close-packed RuNPs. This [Ru<sub>5</sub>] model displays 11 CO ligands, all of them in terminal position, as follows: three CO molecules are coordinated on the ruthenium atom in the top of the pyramid, while two CO ligands coordinate on each of the four atoms of the square base (see Figure 3e). The [Ru<sub>5</sub>] carbonyl cluster also exhibits a  $\mu_5$ -carbide which is both coordinated to the four Ru atoms of the square facet and to the Ru atom in top of the pyramid. This coordination mode mimics the one observed for

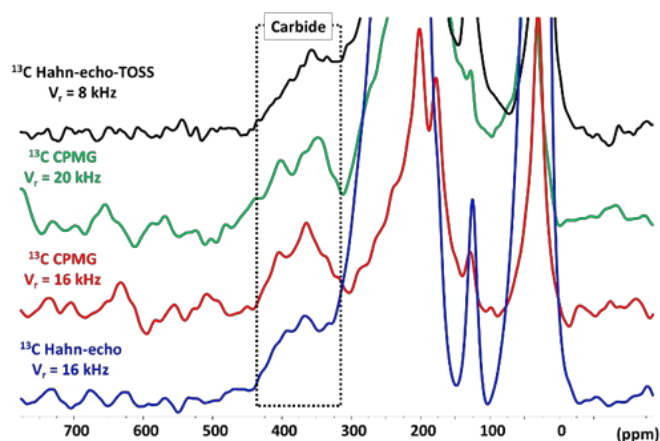


**Figure 2.** Vertical expansion of the signal at *ca.* 360 ppm of <sup>13</sup>C MAS NMR spectra of Ru/PVP<sub>ac</sub> with Hahn-echo at 16 kHz, CPMG (summed echoes) at 16 kHz and 20 kHz and Hahn-echo TOSS at 8 kHz protocols. All spectra were acquired with a 3.2 mm rotor except the Hahn-echo TOSS that was done with a 4 mm rotor. Full spectra are presented in the ESI (Figure S2).

$\mu_5$ -carbides on the larger  $\text{Ru}_{55}\text{NP}$  model (*i.e.* intermediate **f** in Figure 5).

Several  $[\text{Ru}_5](\text{CO})_x$  ( $x = 0-4$ ) and  $[\text{Ru}_5](\text{CO})_x(\text{OH}_2)$  ( $x = 0-3$ ) clusters are obtained from  $[\text{Ru}_5]$  by adding CO and/or  $\text{H}_2\text{O}$  ligands. The carbide resonances computed for these model clusters are depicted in Figure 3. As it can be noticed, chemical shifts of the carbide depend on the number of ligands coordinated around the square facet, in line with the screening effect of the CO  $\pi$  electrons. But it is never weaker than 382 ppm. The  $\mu_5$ -carbide in the  $[\text{Ru}_5]$  cluster, *i.e.* with no shielding by surface species, displays a computed  $^{13}\text{C}$  NMR resonance at *ca.* 502 ppm (Figure 3e). The estimated  $\delta$  value is of about 487 ppm upon coordination of a new CO ligand on one of the ruthenium atoms of the facet (*i.e.*  $[\text{Ru}_5](\text{CO})$  model, Figure 3d). After addition of two and three CO ligands on the square facet of the  $[\text{Ru}_5]$  cluster the calculated chemical shifts for the  $\mu_5$ -carbides are of 429 ppm and of 396 ppm (Figures 3b and 3c). It changes to 382 ppm if the same facet is saturated with a fourth CO ligand as in the case of the  $[\text{Ru}_5](\text{CO})_4$  model (Figure 3a). This  $[\text{Ru}_5](\text{CO})_4$  cluster may be seen as a scale model as close as possible to a RuNP under syngas exposure, which is most likely fully covered with COs. It must also be stressed that, on the larger  $\text{Ru}_{55}\text{NP}$  model employed in the DFT mechanistic study below, under realistic surface composition carbides are surrounded by CO molecules, in line with this  $[\text{Ru}_5](\text{CO})_4$  model cluster. For instance, species **f** in Figure 5 displays in the vicinity of the carbide at least four CO ligands binding the terminal

positions of the 4-fold site containing the  $\mu_5$ -carbide. The replacement of one CO ligand in the  $[\text{Ru}_5](\text{CO})_4$  cluster by a water molecule involves an up-field shift of the carbide signal by 11 ppm (393 ppm vs. 382 ppm, see Figure 3i). Thus, the experimental resonance at *ca.* 360 ppm on the  $^{13}\text{C}$  NMR spectrum can probably be attributed to a  $\mu_5$ -carbide surrounded by at least four CO ligands capping the terminal positions around the square facet. In addition,  $[\text{Ru}_4]$  and  $[\text{Ru}_6]$  model clusters are employed in the present DFT-GIAO NMR study in order to compute  $^{13}\text{C}$  chemical shifts for  $\mu_3$ -carbides in several environments (see Figures S7 and S9 in the ESI and related discussion on their structural features). Thus, model  $[\text{Ru}_4]$  and  $[\text{Ru}_6]$  clusters aim at reproducing the three-fold sites of RuNPs. Computed chemical shifts for the  $\mu_3$ -carbides on several  $[\text{Ru}_4](\text{CO})_x$  ( $x = 0-3$ ) and  $[\text{Ru}_4](\text{CO})_x(\text{OH}_2)$  ( $x = 0-2$ ) clusters range in-between 445 and 485 ppm, while the shifts for similar  $\mu_3$ -carbides on  $[\text{Ru}_6](\text{CO})_x$  ( $x = 0, 1$ ) and  $[\text{Ru}_6](\text{OH}_2)$  models in-between 433 and 463 ppm. Hence, on both model clusters the computed  $^{13}\text{C}$  shifts for the  $\mu_3$ -carbide are far from the 360 ppm experimental resonance. However, in order to do an unequivocal assignment of the 360 ppm experimental resonance to a  $\mu_5$ -carbide, it is necessary to calculate the  $^{13}\text{C}$  NMR signal of species that can be formed from the carbide in the presence of  $\text{H}_2$  and CO molecules. The  $^{13}\text{C}$  NMR chemical shifts calculated for methine (CH), methylene ( $\text{CH}_2$ ) and ketylenidene (CCO) on  $[\text{Ru}_5](\text{CO})_4$  model clusters are

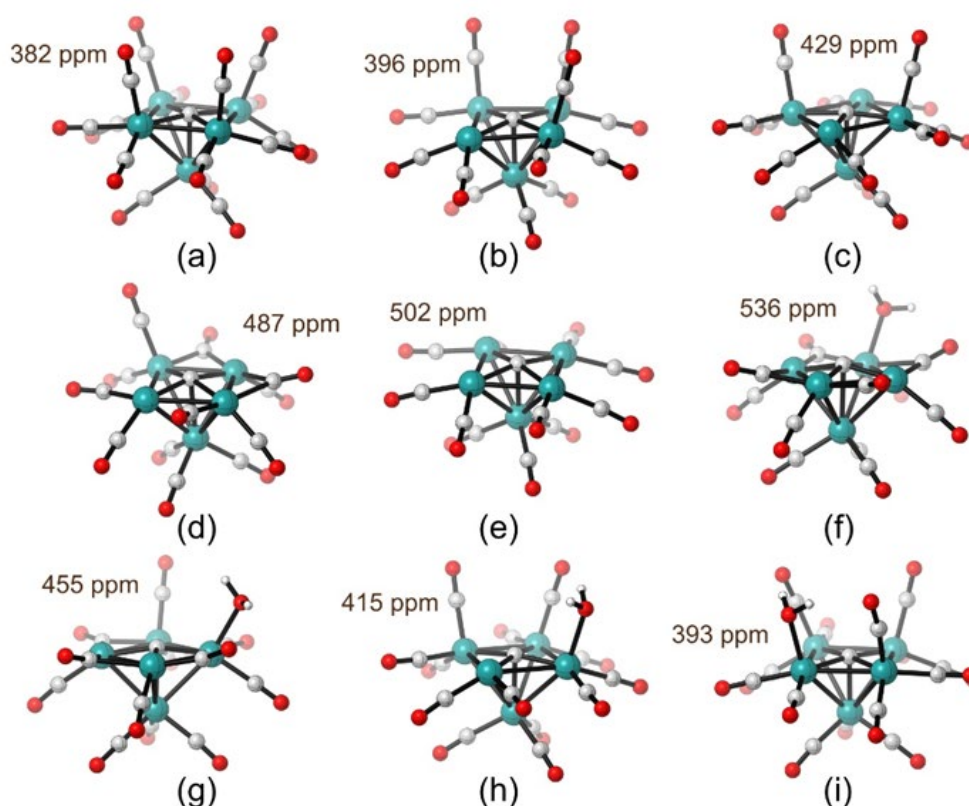


**Figure 3.** Computed  $^{13}\text{C}$  carbide chemical shift for several  $[\text{Ru}_5]$  model clusters: (a)  $[\text{Ru}_5](\text{CO})_4$ ; (b)  $[\text{Ru}_5](\text{CO})_3$ ; (c)  $[\text{Ru}_5](\text{CO})_2$ ; (d)  $[\text{Ru}_5](\text{CO})$ ; (e)  $[\text{Ru}_5]$ ; (f)  $[\text{Ru}_5](\text{OH}_2)$ ; (g)  $[\text{Ru}_5](\text{CO})(\text{OH}_2)$ ; (h)  $[\text{Ru}_5](\text{CO})_2(\text{OH}_2)$ ; (i)  $[\text{Ru}_5](\text{CO})_3(\text{OH}_2)$ .



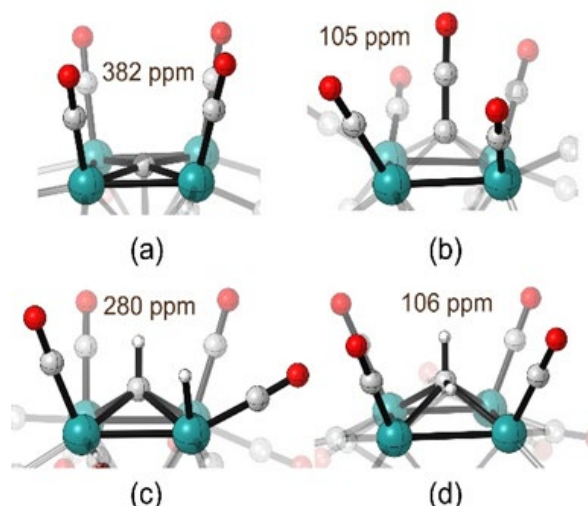


**Figure 4.** Computed chemical shifts of (a) carbide, (b) methine, (c) methylene and (d) ketenylidene species adsorbed on a 4-fold site of model  $[Ru_5](CO)_4$  cluster.

summarized in Figure 4. Thus, the hydrogenation of the carbide leading first to a methine derivative, and then to a methylene one, induces strong shielding of the carbon atom within these species, calculated shifts being of 102 ppm (Figure 4c) and 276 ppm (Figure 4d) with respect to (w.r.t.) the  $\delta$  value computed for the carbide (382 ppm, Figure 4a). A similar trend is observed by the formation of a ketenylidene ligand, for which a calculated  $\delta$  value of about 105 ppm is obtained. Additionally, computed  $^{13}C$  NMR shifts of 3-fold coordinated CH, CH<sub>2</sub> and CCO species on model  $[Ru_4](CO)_3$  clusters reveal  $\delta$  values of 303 ppm, 195 ppm and 110 ppm (Figure S8), whilst the same  $\mu_3$  intermediates adsorbed on  $[Ru_6](CO)$  models display computed values of 314 ppm, 193 ppm and 118 ppm (Figure S9). Thus, the experimental chemical shift of about 360 ppm cannot be attributed to an adsorbed methine, methylene or ketenylidene intermediate. Moreover, according to the present calculations as well as to other studies,<sup>52</sup> the CO chemical shift cannot be so unshielded. The 360 ppm value is a clear signature of a  $\mu_5$ -surface carbide.

#### DFT mechanistic investigations

DFT investigations of several carbide formation pathways are carried out on a  $Ru_{55}$  NP model of about 1 nm. This  $Ru_{55}$  nanoparticle intends to replicate experimental conditions such as size, shape and surface composition. Under syngas exposure, the ruthenium surface is saturated with CO ligands, in line with our previous DFT/GC-MS study,<sup>37</sup> with a calculated ratio of 1.5 CO molecules per surface ruthenium atom (*i.e.*  $Ru_{55}(CO)_{66}$ ). This  $Ru_{55}(CO)_{66}$  model is further employed in the present DFT mechanistic study. While at high surface coverage the direct CO bond cleavage is less probable to occur,<sup>31,38,40</sup> we first assess carbide formation by hydrogen assisted routes involving COH\* intermediates. These mechanistic investigations are carried out in several types of sites which are present on the surface of our RuNP model. As already recalled in the Introduction, dihydrogen adsorption on the surface of RuNPs is low during CO

hydrogenation. Aiming at reproducing a realistic surface composition in the present DFT mechanistic study, but at the same time taking into account that hydroxymethylidyne dissociation routes require co-adsorbed H\* species in order to occur, we further suggest a reversible adsorption of dihydrogen in very small amounts on the ruthenium surface at specific sites. As already pointed out above, we might associate the H<sub>2</sub> co-adsorption with a thermodynamic driving force which accompanies the exothermic formation of stable carbide-water intermediates on the surface. Therefore, in the following COH mechanisms, we consider the  $Ru_{55}(CO)_{66}H_2$  NPs as starting structures, dihydrogen being coordinated by turn in several sites on the model  $Ru_{55}(CO)_{66}$  NP. The relative energies of the intermediates computed in the hydroxymethylidyne mechanisms are calculated w.r.t the separated  $Ru_{55}(CO)_{66}$  and H<sub>2</sub>(g) species, which is set as a reference system (0 kcal mol<sup>-1</sup>, see Figures 5, 8, 9, 10 and Figures S11, S12).

We first show that stable carbides can be formed within 4-fold sites of a 101 face on the model NP (Figure 5). The first step consists in the adsorption of dihydrogen on the CO-saturated surface. This process is slightly endothermic (2.6 kcal mol<sup>-1</sup>), leading to intermediate **a**. The COH\* intermediate is formed in the next step as one  $\mu$ -CO ligand migrates to a four-folded site concomitant with the transfer of one of the co-adsorbed hydrogen atoms towards the oxygen-end of the migrating CO\* molecule. This reaction occurs with a low barrier (12.5 kcal mol<sup>-1</sup>, according to the computed energy of **TS<sub>a-b</sub>**) yielding a slightly more stable COH\* intermediate **b**, which has a relative energy of -3.9 kcal mol<sup>-1</sup> w.r.t the separated reactants. The transfer of the second hydride to the O atom of COH\* intermediate occurs at the reasonable kinetic cost of 27.1 kcal mol<sup>-1</sup> (see **TS<sub>b-c</sub>**), and provokes the C-O bond dissociation. The resulting compound **c** consists in a ruthenium carbide that lies in the surface, while water remains in the vicinity of the surface owing to possible hydrogen bond formation with the adsorbed COs. The COH\* + H\*  $\rightarrow$  C\* + H<sub>2</sub>O transformation is exothermic by 10.6 kcal mol<sup>-1</sup>. The carbide is coordinated to the ruthenium framework in a  $\mu_5$  fashion involving four surface and one core Ru atoms (the bonding pattern is illustrated in Figure 5). Water can subsequently coordinate to the ruthenium surface yielding highly stable intermediates, **d**. The possible presence of such carbide-water species on the surface of RuNPs had been highlighted in our preceding DFT studies,<sup>37</sup> but no mechanistic study had been performed in order to assess the kinetic accessibility of this product. Water release in the medium is endothermic by 12.2 kcal mol<sup>-1</sup>, whereas further stabilization of the carbide intermediate **e** is obtained by adsorption of another CO molecule in the vacancy created by water departure, formation of species **f** being highly exothermic (-29.9 kcal mol<sup>-1</sup> w.r.t intermediate **e**). Thus, we show here that stable ruthenium carbides are obtained under realistic experimental conditions through COH\* species, on 4-fold sites on the 101 flat terraces of RuNPs and not only on steps, which are not expected to be present in high

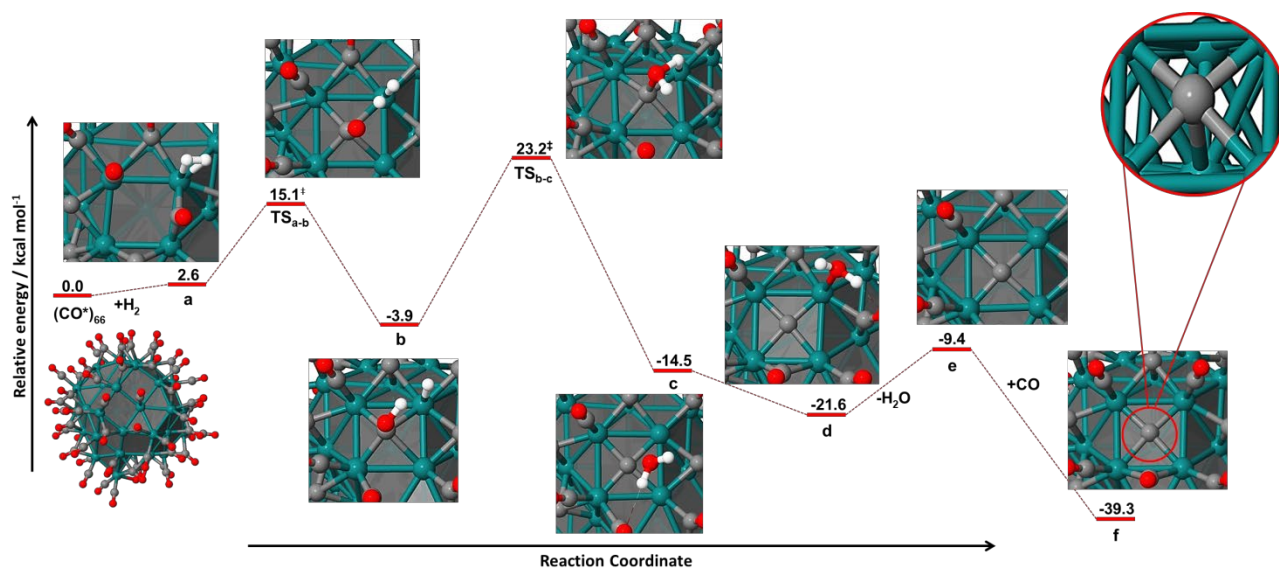


**Figure 5.** Carbide formation via hydroxymethylidyne pathway in a 4-fold site on the 101 face of the model  $\text{Ru}_{55}(\text{CO})^*_{66}\text{H}^*_2\text{NP}$ .

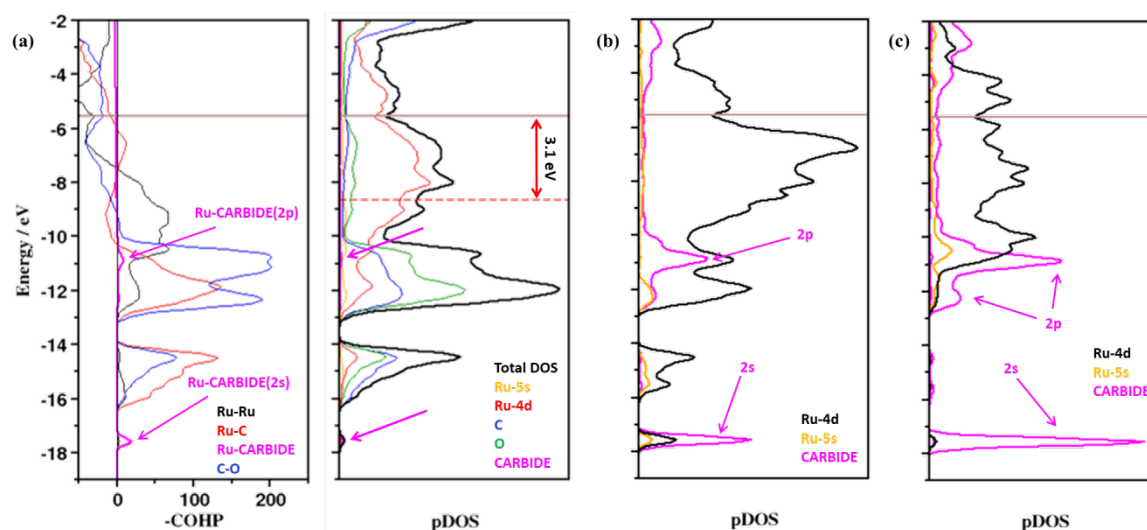


**Figure 6.** (a) pCOHP( $\epsilon$ ) and pDOS( $\epsilon$ ) profiles for intermediate **e** (*i.e.*  $\text{Ru}_{55}\text{CO}^*_{65}\text{C}^*$ ); the metal d-band center (dashed red line) is situated at *ca.* 3.1 eV below the Fermi level (brown line). (b) pDOS( $\epsilon$ ) profile highlighting the interaction of the surface carbide with neighboring in-plane surface Ru atoms. (c) pDOS( $\epsilon$ ) profile highlighting the interaction of the surface carbide with the vicinal core Ru atom.

concentration on 1 nm NPs. In addition, these mechanistic achievements complement previous DFT studies in the field,<sup>31,38–41</sup> according to which CO hydrogenation reactions occurring on the terraces of RuNPs proceed exclusively via formyl (HCO) intermediates, lacking thus to form carbides during the CO dissociation step.

The chemical bonding formed between the surface carbide in intermediate **e** (*i.e.*  $\text{Ru}_{55}\text{CO}^*_{65}\text{C}^*$  species) and the neighboring ruthenium atoms is also assessed. Projected density of states (pDOS) and crystal orbital hamilton population (pCOHP) profiles are computed in this respect (Figure 6). The signature of the carbide is highlighted and consists in two bands: one at about -11 eV (corresponding to the 2p orbitals on the carbide), the other band being situated at *ca.* -17.5 eV (the 2s orbitals on the carbide). Computed pCOHP and pDOS profiles of co-adsorbed

CO molecules are also displayed (blue and green lines in Figure 6a). However, a more detailed analysis<sup>37</sup> on the adsorption of CO ligands at the surface of ruthenium nanoparticles was previously carried out on the same  $\text{Ru}_{55}(\text{CO})^*_{66}$  model. Figure 6b highlights bonding interactions between the carbide and the neighboring surface ruthenium atoms, whereas according to the plotted pDOS profile in Figure 6c, the chemical bond between the carbide and the proximal core ruthenium atom is weaker. Yet, these findings are in line with previous studies<sup>4</sup> performed on cobalt carbides, which emphasize weak interactions between the surface carbides and the core metal atoms. Nevertheless, adsorption of another CO molecule (or even a  $\text{H}_2\text{O}$  one) in the vicinity of ruthenium carbide in intermediate **e**, strengthens the adsorption of the carbide to the core Ru atom. Hence, the calculated Ru(core)-C(carbide) length

in intermediate **f** (*i.e.*  $\text{Ru}_{55}\text{CO}^*_{65}\text{C}^*\text{CO}^*$ ) is significantly shorter than the one in species **e** (2.07 Å in **f** vs. 2.25 Å in **e**), indicating thus a significantly stronger interaction between the carbide and the core ruthenium atoms in the case of species **f**. On the other hand, calculated charges for intermediate **e** are of -0.71e in the case of the carbide and of +0.46e to +0.60e for the vicinal ruthenium atoms, emphasizing thus a highly ionic character of these Ru-C bonds. A detailed charge map of the  $\text{Ru}_{55}\text{CO}^*_{65}\text{C}^*$  species **e** is illustrated in Figure S10.

Formation of  $\mu_5$ -carbides in the tip- $\text{B}_5$  defect site on the  $\text{Ru}_{55}(\text{CO})^*_{66}(\text{H})^*_2$  model NP is additionally assessed through hydroxymethylidyne pathways. Two competitive routes were revealed by DFT calculations, one occurring through ( $\text{C}^*$ ,  $\text{OH}_2^*$ ) intermediates (Figure S11) whereas the other involving ( $\text{C}^*$ ,  $\text{OH}^*$ ) species (Figure S12). Computed relative energies of intermediates **d**<sup>1</sup> ( $\text{C}^*$ ,  $\text{OH}_2^*$ ) and **k**<sup>2</sup> ( $\text{C}^*$ ,  $\text{OH}^*$ ) are of -38.6 kcal mol<sup>-1</sup> and of -15.7 kcal mol<sup>-1</sup> w.r.t.  $\text{Ru}_{55}(\text{CO})^*_{66} + \text{H}_2(\text{g})$  reference. For both mechanisms, the highest barrier corresponds to  $\text{CO}^* + \text{H}^* \rightarrow \text{COH}^*$  transformation (29.5 kcal mol<sup>-1</sup>, this step being common for both pathways), whereas formation of both ( $\text{C}^*$ ,  $\text{OH}_2^*$ ) and ( $\text{C}^*$ ,  $\text{OH}^*$ ) species from  $\text{COH}^*$  intermediates occurs with lower barriers, 16.2 kcal mol<sup>-1</sup> and 18.2 kcal mol<sup>-1</sup> respectively. However, both mechanisms lead to the same final product, intermediate **e**<sup>1</sup>, a  $\mu_5$ -surface carbide lying at the bottom of the  $\text{B}_5$  site (Figures 7, S6 and S7). The binding mode of the  $\mu_5$ -carbide in species **e**<sup>1</sup> is similar to the one emphasized for the  $\mu_5$ -carbide adsorbed in a 4-fold site on the 101 face of the RuNP (see for comparison intermediate **f** in Figure 5). It is also worth noting that formation of ( $\text{C}^*$ ,  $\text{OH}^*$ ) species in  $\text{B}_5$ -like step sites was previously<sup>31</sup> suggested by ab-initio molecular dynamics studies (AIMD). Nevertheless, the high number of adsorbed hydrides (adsorbed  $\text{CO}^*:\text{H}^*$  ratios of 2:1 and 3:1, significantly higher than realistic surface composition under syngas exposure) and

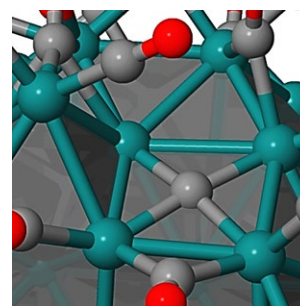


**Figure 7.** Surface  $\mu_5$ -carbide adsorbed at the bottom of the  $\text{B}_5$  site on the model RuNP (intermediate **e**<sup>1</sup> – see Figures S11 and S12 for related formation routes); the carbide binds to four surface and one core ruthenium atoms.

the use of slab models in the AIMD calculations may hamper direct comparisons with the actual study.

Given that 3-fold adsorption sites, of hcp and fcc type, are the most abundant ones on the surfaces of small RuNPs, we also assess the possibility of yielding  $\mu_3$  carbides. Even though, according to the DFT-GIAO NMR calculations performed on model  $[\text{Ru}_4]$ ,  $[\text{Ru}_5]$  and  $[\text{Ru}_6]$  clusters, the 360 ppm <sup>13</sup>C signal is most probably attributed to a  $\mu_5$  carbide and not to a  $\mu_3$  one, further information regarding the thermodynamic and kinetic accessibility of such  $\mu_3\text{-C}^*$  species might lead to better understanding of carbide formation on the surface of RuNPs. A proposed DFT mechanism concerning the formation of  $\mu_3$ -carbides via hydroxymethylidyne intermediates is illustrated in Figure 8. Thus, adsorption of a hydrogen molecule on the CO-saturated surface of the model RuNP is slightly endothermic, leading to intermediate **a**<sup>3</sup>. Subsequent transformation, the transfer of one of the surface  $\text{H}^*$  to the oxygen-end on the  $\text{CO}^*$  molecule subjected to cleavage, displays a calculated barrier of 26.5 kcal mol<sup>-1</sup> w.r.t species **a**<sup>3</sup>. The  $\text{COH}^*$  intermediate, **b**<sup>3</sup>, is thus formed. The second transformation

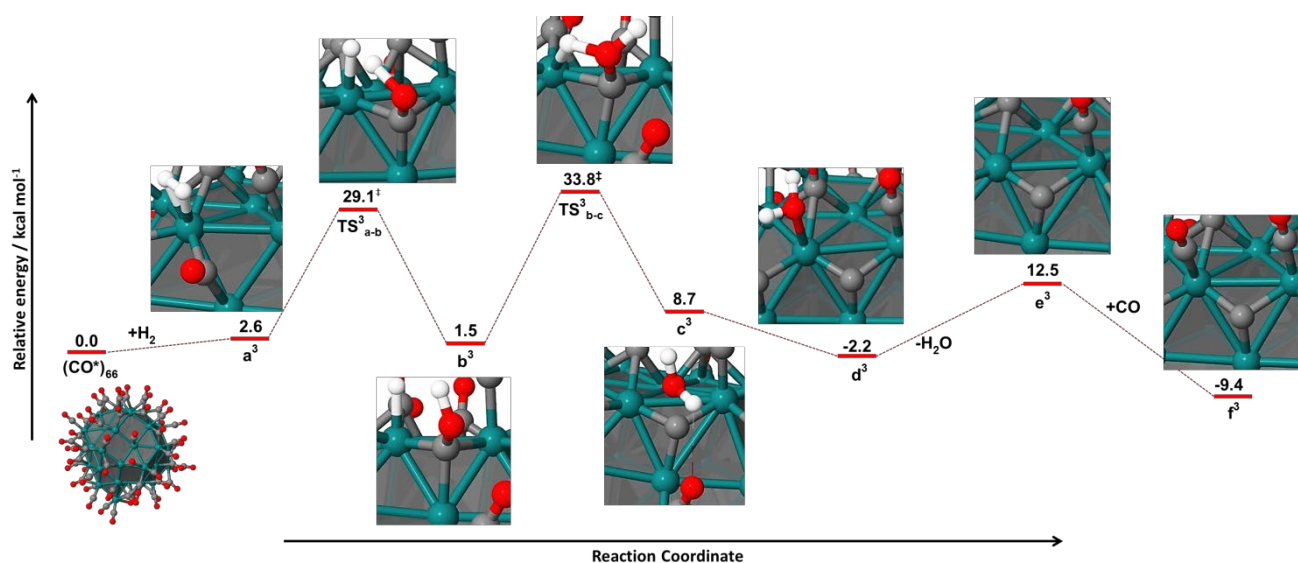


**Figure 8.** Hydroxymethylidyne pathway leading to the formation of  $\mu_3$ -carbide in a 3-fold site on the  $\text{Ru}_{55}(\text{CO})^*_{66}(\text{H})^*_2$  NP model; the carbides in intermediates **c**<sup>3</sup>–**f**<sup>3</sup> lie above the ruthenium surface.



consists in the transfer of the second surface  $H^*$  to the  $COH^*$  species, reaction occurring with a calculated barrier of  $32.3 \text{ kcal mol}^{-1}$  w.r.t **b**<sup>3</sup>. It results in a  $\mu_3$ -carbide lying above the ruthenium surface, accompanied with a water molecule hydrogen-bonded to the adsorbed CO ligands (intermediate **c**<sup>3</sup>). The formation of such a ( $\mu_3\text{-C}^*$ ,  $H_2O$ ) intermediate is endothermic by  $8.7 \text{ kcal mol}^{-1}$ , in sharp contrast to that of ( $\mu_5\text{-C}^*$ ,  $H_2O$ ) species which are highly stable, according to calculated reaction energies (see Figures 5, 10 and S6 for comparisons). However, further stabilization of intermediate **c**<sup>3</sup> is achieved by water coordination in the vicinity of the  $\mu_3$ -carbide, formation of **d**<sup>3</sup> being slightly exothermic w.r.t. to the reference system (*i.e.*  $Ru_{55}CO^*_{66} + H_2$ ), in particular thanks to the hydrogen bonds formed between the adsorbed water molecule and the co-adsorbed CO groups. Water release in the medium leads to a less stable species, **e**<sup>3</sup> ( $14.7 \text{ kcal mol}^{-1}$  w.r.t intermediate **d**<sup>3</sup>), whereas coordination of an extra CO molecule nearby the  $\mu_3$ -carbide brings further stabilization, formation of species **f**<sup>3</sup> being highly exothermic w.r.t intermediate **e**<sup>3</sup> ( $-21.9 \text{ kcal mol}^{-1}$ ). Another proposed mechanism features  $\mu_6$ -carbide formation within the tip, via  $COH^*$  intermediates (Figure 9). The adsorption of a hydrogen molecule in the  $B_5$  site can trigger the rearrangement of the neighboring  $CO^*$  molecules in the  $B_5$ -tip site (w.r.t. our initial model); this reversible rearrangement is apparently exothermic, leading to intermediate **a**<sup>4</sup>. The next transformation goes via a low-lying TS (see **TS**<sup>4</sup><sub>a-b</sub>), which mainly differs from **a**<sup>4</sup> by a shorter (CO)--- $\eta$ -H bond length. The resulting  $\mu\text{-COH}^*$  intermediate, **b**<sup>4</sup>, can undergo a reversible isomerization to a  $\mu_4\text{-COH}^*$  species together with Ru-Ru bond cleavage (intermediate **b'**<sup>4</sup>). Subsequent step consists in the carbide formation, the TS associated to this transformation being the highest-lying TS of this mechanism with a calculated value of  $19.6 \text{ kcal mol}^{-1}$  (see **TS**<sup>4</sup><sub>b'-k</sub>). It is also worth noting that the activation barriers computed for this pathway are lower

than  $20 \text{ kcal mol}^{-1}$ , making it the pathway with the lowest barriers among all investigated mechanisms throughout this study. The highly stable intermediate **k**<sup>4</sup> consists in a  $\mu_6$ -carbide formed under the tip Ru atom in the presence of a  $\mu\text{-OH}^*$  group. Finally, the adsorbed  $\mu\text{-H}^*$  species is transferred to the  $OH^*$  group at a reasonable kinetic cost of  $14.2 \text{ kcal mol}^{-1}$  (see **TS**<sup>4</sup><sub>k-d</sub>) leading to the formation of a more stable water-carbide intermediate ( $\mu_6\text{-C}^*$ ,  $H_2O^*$ ), such as the one depicted in this pathway (intermediate **d**<sup>4</sup>). Water departure in the medium, leading to the formation of **e**<sup>4</sup>, is slightly endothermic ( $7.5 \text{ kcal mol}^{-1}$  w.r.t **d**<sup>4</sup>). To our knowledge, this is the first example of  $\mu_6$ -carbide highlighted on RuNPs, similar examples being known only in the molecular chemistry of ruthenium clusters.<sup>42</sup> But it occurs on the tip- $B_5$  site, which can be considered as a special site scarcely present at the surface of RuNPs.

We also found a competitive pathway on the same site, which turns out to be an unexpected and very interesting side result. We indeed observed the formation of a highly stable ruthenium molecular complex on the surface of the NP. Rearrangement of the surface metal atoms occurs in the proximity of the  $B_5$  site, with the cleavage of some Ru-Ru bonds. It results in a  $\mu\text{-Ru}$  atom coordinated to the  $Ru_{54}$  remaining cluster, reminiscent of a pseudo-octahedral molecular complex on the NP surface (Figure 10e<sup>5</sup>). To the best of our knowledge it represents the first example of such a surface complex reported so far on RuNPs. In order to understand the stability and the chemical bonding of such an unusual species, we further compare this surface complex with a reference 18-electron  $Ru(CO)_4H_2$  molecular system (Figure S13). According to computed pDOS profiles on both species, the d-band structure pattern of the central Ru atom in the surface complex replicates to a high extent the one corresponding to the Ru atom in the  $Ru(CO)_4H_2$  reference

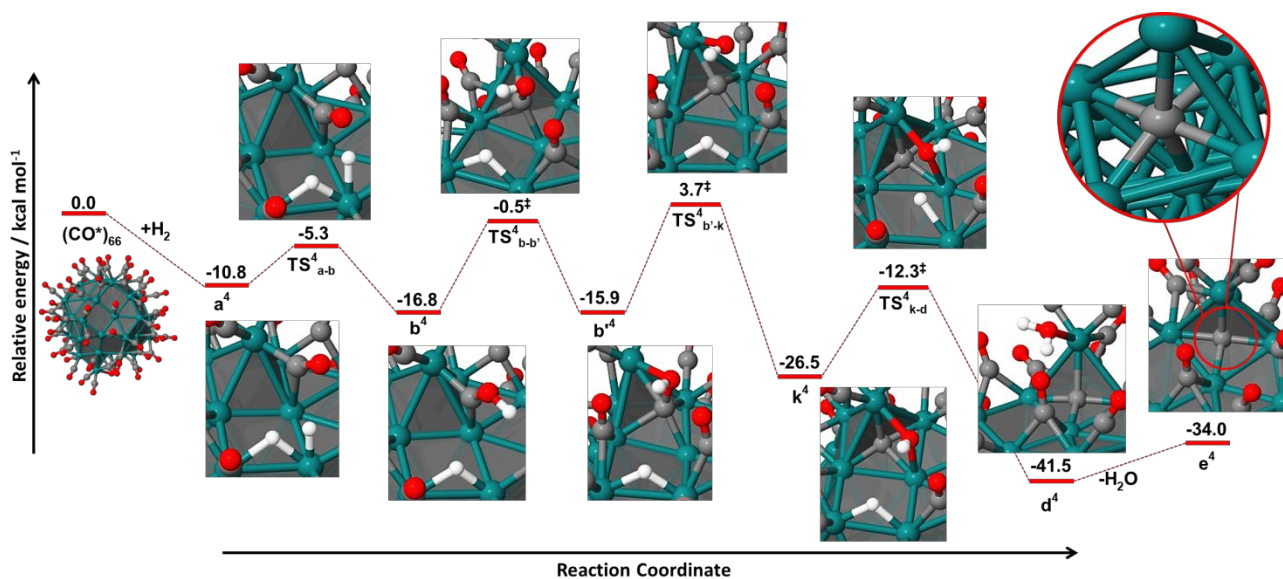


**Figure 9.** Hydroxymethylidyne route leading to the formation of  $\mu_6$ -carbide into the tip- $B_5$  site of the model  $Ru_{55}(CO)^*_{66}H^*_2$  NP.



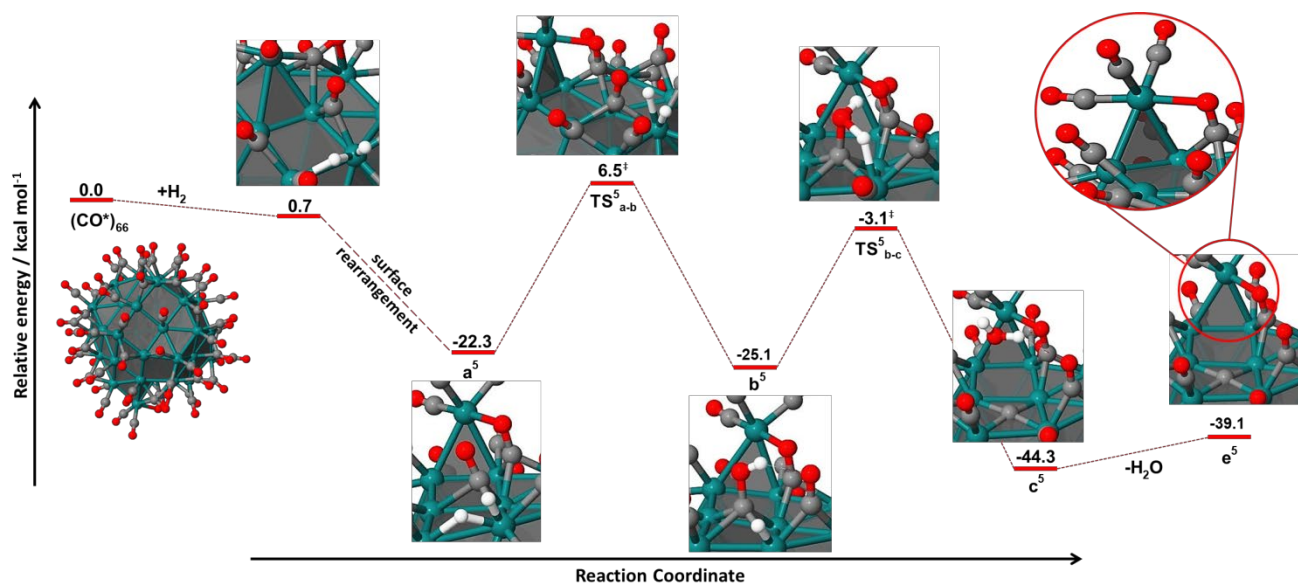


**Figure 10.** Formation of  $\mu_5$ -carbide in a standard 4-fold site; the reaction occurs in the vicinity of a surface ruthenium molecular complex, obtained by surface rearrangement at the tip-Ru atom.

system (see Figure S14 and related discussion in the ESI). Charge analyses on both structures indicate as well a good correlation between the charge computed for the Ru atom in the surface species (+0.75e) and the one for the Ru atom in the molecular complex (+0.93e). Thus, this peculiar surface species can be viewed as a  $\text{Ru}(\text{CO})_3(\text{OC})\text{Ru}_{54}$  complex.

Figure 10 also depicts the COH pathway leading to a  $\mu_5$ -carbide adsorbed in a 4-fold site in the vicinity of the surface molecular complex. The possibility of obtaining such surface complexes may involve stabilization and favor  $\text{H}_2$  co-adsorption. Hence, and despite Ru-Ru bond breaking, intermediate  $\mathbf{a}^5$  is highly stable compared to the reference system. Formation of the COH\* intermediate implies the transfer of one  $\text{H}^*$  to the CO\* ligand along with the migration of the CO\* molecule (see  $\text{TS}_{\mathbf{a-b}}^5$ ), which is the highest activation barrier calculated for this mechanism. However, a 28.8 kcal.mol $^{-1}$  barrier height can be overcome under quite mild conditions. The COH\* species obtained in  $\mathbf{b}^5$  is further stabilized by hydrogen bonding formed with co-adsorbed CO\* ligands, as well as the  $\text{TS}_{\mathbf{b-c}}^5$  corresponding to carbide and water formation. However, formation of the surface carbide-molecular complex species in  $\mathbf{e}^5$ , following water release in the medium, is slightly endothermic. The carbides in intermediates  $\mathbf{c}^5$  and  $\mathbf{e}^5$  are coordinated to the RuNP in a fashion that was previously discussed for the other  $\mu_5$ -carbide examples (for comparisons see Figures 5, 7 and 10). Thus, we show in this DFT mechanistic study that formation of stable  $\mu_5$ -carbides can be achieved via COH intermediates in any available 4-fold site on the surface of the RuNP, and not only in sites displaying specific motifs, such as the  $\text{B}_5$  ones.

The direct CO dissociation mechanism is also assessed as an alternative route for carbide formation on our  $\text{Ru}_{55}(\text{CO})_{66}^*$  NP. Previous studies by several groups on various Ru models<sup>30,33,36</sup> highlighted that this direct dissociation route occurs

preferentially in defective sites of the  $\text{B}_5$  or  $\text{B}_6$  type. Thus, earlier DFT explorations carried out on a  $\text{Ru}_{57}$  NP,<sup>30</sup> which is similar in terms of size with the  $\text{Ru}_{55}$  model employed in the present study, revealed that the direct dissociation route for a CO molecule adsorbed in the  $\text{B}_5$  site requires a reaction energy of ca. 11 kcal mol $^{-1}$  and a barrier height of about 24 kcal mol $^{-1}$ . Yet, the surface coverage of ca. 1.0 CO ML in the case of the  $\text{Ru}_{57}$  model is lower than the ca. 1.5 ML CO displayed by our  $\text{Ru}_{55}(\text{CO})_{66}^*$  NP. Here, we illustrate a computed direct CO dissociation mechanism occurring into the tip- $\text{B}_5$  site as well (Figure S15). We find that this transformation is endothermic by 16.4 kcal mol $^{-1}$ , and requires activation energy of 34.5 kcal mol $^{-1}$ . Hence, both the reaction energy and the activation barrier are higher on our  $\text{Ru}_{55}$  model compared to the  $\text{Ru}_{57}$  one. These differences are most probably related to an increased surface coverage in the case of the  $\text{Ru}_{55}$  NP (1.5 ML CO) compared to the  $\text{Ru}_{57}$  one (1.0 ML CO). Similar observations were indicated by other DFT studies, according to which direct dissociation routes are less probable to occur on saturated surfaces due to increased lateral repulsions between the adsorbed CO ligands and the  $\text{C}^*$  and  $\text{O}^*$  species.<sup>31,38,40</sup> Thus, carbide formation via the direct dissociation route on the  $\text{Ru}_{55}(\text{CO})_{66}^*$  NP model, at high CO surface coverage, is highly endothermic, in sharp contrast to their formation through hydroxymethylidyne pathways. Moreover, the activation energy of the direct dissociation route on the  $\text{Ru}_{55}$  NP is also higher than those computed for the COH ones. For example, calculated gaps between the barrier heights of the direct dissociation pathway and those of the COH mechanisms leading to  $\mu_5$ -carbides are of 5.0–7.4 kcal mol $^{-1}$  (for energy comparisons see Figures 5, 10, S11 and S15). Besides the route depicted in Figure S15, we also investigated this direct dissociation pathway on other adsorption sites on the same  $\text{Ru}_{55}(\text{CO})_{66}^*$  NP model. However, the DFT explorations suggest that the direct dissociation of a CO

molecule is less likely to occur within 4-fold and 3-fold sites on the terraces of RuNPs.

Given that ruthenium carbides could have interesting implications in more complex processes such as the FTS, we additionally assess here by means of DFT explorations their possible transformation into methylene ( $\text{CH}_2^*$ ) and ketenylidene ( $\text{CCO}^*$ ) species, but without considering the kinetic accessibility of these products (see Figures S16–S19 and related discussions in the ESI). According to the computed energies, the  $\text{Ru}_{55}(\text{CO})^*_{65}\text{C}^*\text{H}^*_2 \rightarrow \text{Ru}_{55}(\text{CO})^*_{65}(\text{CH}_2)^*$  and  $\text{Ru}_{55}(\text{CO})^*_{65}\text{C}^*\text{CO}^* \rightarrow \text{Ru}_{55}(\text{CO})^*_{65}(\text{CCO})^*$  reactions are exothermic only w.r.t.  $\mu_3$ -carbides (Figure S18). As for  $\mu_5$ -carbides, the same transformations are endothermic in all cases, most probably due to the increased stability of these penta-coordinated  $\text{C}^*$  species (Figures S16, S17 and S19). Hence, based on computed DFT energies of possible products obtained from carbides by hydrogenation or C-C coupling reactions, we further emphasize the enhanced stability of the  $\mu_5$ -carbides. On the other hand, in order to understand whether surface carbides have direct implication within the ruthenium-catalyzed FTS, a more exhaustive mechanistic investigation is required. Consideration of that kind of study is in progress in our group.

## Conclusions

Even though the existence of ruthenium carbides was proposed long time ago, the present study brings further clarification and reveals that such species can be easily formed in mild conditions on pure and ultra-small RuNPs during CO hydrogenation. Although their NMR signals are difficult to observe (use of labelled  $^{13}\text{C}$ , broad and weak resonance) we show that with the CPMG protocol, these species can be detected relatively quickly. According to DFT-GIAO NMR calculations, performed on  $[\text{Ru}_4]$ ,  $[\text{Ru}_5]$  and  $[\text{Ru}_6]$  model clusters, the 360 ppm experimental  $^{13}\text{C}$  NMR signal should be attributed to a surface  $\mu_5$ -carbide and not to a  $\mu_3$  one, nor to another intermediate such as methine, methylene or ketenylidene, possibly formed during CO hydrogenation. The DFT mechanistic investigations, carried out on a  $\sim 1\text{nm}$   $\text{Ru}_{55}$  NP model, which is realistic in terms of size, structure and surface composition, reveal that formation of  $\mu_5$ -carbides is exothermic, and occurs at a reasonable kinetic cost on standard sites of the RuNP via hydroxymethylidyne pathways. Thus, we show that these penta-coordinated carbides are formed in any available 4-fold site on the NP, and not only in defects of the  $\text{B}_5$  or  $\text{B}_6$  type, as previously considered. In contrast to  $\mu_5$ -carbides, which are stable surface species according to computed DFT energies and to  $^{13}\text{C}$  NMR assignments, formation of  $\mu_3$ -carbides through COH intermediates is endothermic, and displays slightly higher barrier heights. Such  $\mu_3$  carbides, if possibly obtained in harsher conditions, would probably react immediately with  $\text{H}_2$  or CO, in line with calculated reaction energies related to these transformations. On the contrary,  $\mu_5$  carbides are more stable towards hydrogenation or chain growth reactions. Carbide formation by direct dissociation routes is less probable to occur on a CO-crowded surface, which is realistic in terms of coverage.

Calculated reaction energies and activation barriers for the direct dissociation mechanism on our  $\text{Ru}_{55}$  NP confirm this assumption. The DFT explorations also suggest that  $\mu_6$ -carbides, reported previously for molecular ruthenium clusters only, can be easily obtained within the tip  $\text{B}_5$  site of the model Ru nanoparticle via COH routes. In addition, possible formation at the same tip atom of a surface pseudo-octahedral molecular complex of the  $\text{Ru}(\text{CO})_3(\text{OC})\text{Ru}_{54}$  type, consisting in a  $\mu$ -Ru atom coordinated to the remaining RuNP moiety, may involve further stabilization, favoring the adsorption of dihydrogen on the surface, and the subsequent hydrogen-assisted CO bond cleavage, leading thus to carbide formation. Although the experimental work within this study has been achieved at a temperature lower than typical ones for the Fischer-Tropsch synthesis, the present results suggest that the possible presence of carbides should systematically be taken into account in future mechanistic studies of the catalytic activity of RuNPs for FTS.

## Methods

### Experimental section

All manipulations were performed under a dry argon atmosphere using standard Schlenk and vacuum-line techniques. The organic solvents were purified before use under argon atmosphere by filtration on adequate column of a purification apparatus (MBraun). Reagents were purchased from commercial providers and used without further purification.  $\text{Ru}(\text{COD})(\text{COT})$  was purchased from Nanomep Toulouse, CO and  $\text{H}_2$  from Air liquide, CO ( $^{13}\text{C}$ , 99.14%) from Eurisotop and polyvinylpyrrolidone (PVP; average mol wt 10.000) from Sigma-Aldrich. They were used without purification.

**Transmission Electron Microscopy (TEM).** RuNPs were observed by TEM after deposition of a drop of a colloidal solution in THF on a copper grid covered with amorphous carbon. Conventional bright-field images were performed at the UMS-Castaing by using a JEOL JEM 1011 CX-T electron microscope operating at 100 kV with a point resolution of 4.5 Å. The approximation of the particles mean size was made through a manual analysis of enlarged micrographs by measuring a number of particles ( $\sim 100$ ) on a given grid.

**Solid state NMR (MAS-NMR).** Solid-state NMR experiments were recorded at the LCC (Toulouse) on a Bruker Avance IIIHD 400 spectrometer equipped with 3.2 and 4.0 mm probes. Samples were packed into 4 mm or 3.2 mm zirconia rotors inside a glove box. The rotors were spun between 8 and 20 kHz (Vr) at 295 K.  $^{13}\text{C}$  MAS experiments were performed with a recycle delay of 5 s.  $^{13}\text{C}$  CP/MAS spectra were recorded with a recycle delay of 1.5 s and a contact time of 3 ms. Hahn-echo and CPMG scheme were synchronized with the spinning rate.  $^{13}\text{C}$  CPMG were acquired with 22 echoes, a delay between train of  $180^\circ$  pulse of 12 rotor periods and a recycle delay of 5 s. After registering the echo-trains, the echoes were summed up before processing.

**Hydrogen temperature-programmed reduction (TPR-H<sub>2</sub>).** TPR-H<sub>2</sub> study was performed using a quartz reactor connected online to a mass spectrometer (Balzer QMG 220M1). 60 mg of catalyst were flushed with argon at 25 °C for 30 min and then switched to 10 vol % H<sub>2</sub> in Ar flow (14 mL·min<sup>-1</sup>). The reaction was carried out at increasing temperatures (from 25 to 400 °C at a rate of 10 °C·min<sup>-1</sup>). The m/z values used to monitor each product were 44 (CO<sub>2</sub>), 28 (CO and N<sub>2</sub>), 18 (H<sub>2</sub>O), 16 (CH<sub>4</sub>), 15 (CH<sub>4</sub>), 14 (CH<sub>4</sub>), and 2 (H<sub>2</sub>).

**Synthesis of Ru/PVP.** Ru NPs stabilized by PVP were prepared according to our previously described organometallic route,<sup>47,53</sup> but with minor modifications. Specifically, Ru(COD)(COT) (157 mg, 0.50 mmol) was introduced in a Fischer-Porter bottle and left under vacuum for 30 min. A solution of PVP (1g) in THF (60 mL), degassed by freeze-pump cycles, was then added using a transfer tubing. The resulting yellow solution was stirred for 30 min at room temperature, after which the bottle was pressurized under 3 bar dihydrogen and the solution allowed reacting overnight. During this time a black/grey precipitate of Ru/PVP was formed. After elimination of excess dihydrogen the supernatant THF solution was filtrated by cannula. The precipitate was washed with pentane (3 x 30 mL) and dried overnight. Ru content: 8 %.

**Obtention of Ru/PVP after CO hydrogenation conditions (Ru/PVP<sub>ac</sub>).** Following the experimental procedure developed for a model CO hydrogenation catalytic reaction,<sup>48</sup> a Fischer-Porter bottle (80 mL) was filled with 100 mg of Ru/PVP (~ 8% Ru), pressurized with 3 bar of syngas (1:1 molar mixture of H<sub>2</sub> and CO) and heated at 150 °C for 24 h. After that, the Fischer-Porter was depressurized and left to reach at room temperature (r.t.). Finally, the NPs after catalytic conditions (Ru/PVP<sub>ac</sub>) were studied by TEM and solid state MAS NMR.

## Computational details

**The Ru<sub>55</sub> model and other geometry features.** It has previously been published and detailed elsewhere.<sup>37</sup> Briefly, it was shaped by slicing an hcp structure by two (001) planes and (101) planes. A tip has been added in order to introduce one B<sub>4</sub> and one B<sub>5</sub> site. Removing one line of atoms between two (101) planes generates a slightly corrugated facet. Such defects can probably be found on NPs larger than this ultra-small 1nm model. With 11 Ru atoms in the core, the surface area of the DFT-PBE optimized cluster is 258 Å<sup>2</sup>. In order to define the bridging character  $\mu_n$  and the hapticity  $\eta^m$ , we have considered an atom of the ad-ligand as coordinated to a given metal atom when the metal-atom distance is lower than 2.1 Å for H, 2.5 Å for C and 2.3 Å for O.

**Periodic DFT calculations of metal RuNP model,** were performed using the *Vienna ab initio simulation package*, VASP.<sup>54,55</sup>

**Energy calculations.** Spin polarized DFT; exchange-correlation potential approximated by the generalized gradient approach proposed by Perdew, Burke, and Ernzerhof (PBE);<sup>56</sup> projector augmented waves (PAW) full-potential reconstruction;<sup>57,58</sup> PAW data sets for metal atoms treating the (n-1)p, (n-1)d and ns states (*i.e.* 14 valence electrons for Ru); kinetic energy cutoff:

500 eV;<sup>37,59,60</sup>  $\Gamma$ -centered calculations;<sup>61</sup> Gaussian smearing of 0.02 eV width.

**Geometry optimization.** Threshold: residual forces on any direction less than 0.02 eV/Å; super-cell size set to ensure a vacuum space of *ca.* 16 Å between periodic images of metal clusters (for example, 27.0 x 27.0 x 27.5 Å for Ru<sub>55</sub>).

**Calculation of reaction barriers.** Reaction barriers were estimated by the climbing image nudge elastic band (CINEB) method,<sup>62-64</sup> spring force between images: 5 eV; force tolerance of 0.02 eV/Å. The harmonic vibrational modes were systematically calculated in order to distinguish minima and saddle points by using the dynamical matrix code implemented in VASP as well as the VASPTST tools also developed by Henkelman's group.

**Vibrational analysis.** All intermediates and TS have been characterized by a normal mode analysis. IRC-like explorations have been performed for almost all TS – unless for TS that obviously connected the considered minima.

**Electronic structure and charge analysis.** Projected density of states (pDOS) and projected crystal orbital hamilton population (pCOHP) profiles, as well as bond energy analysis were achieved with the Lobster software, using the pbeVASPfit basis.<sup>65-67</sup> Ru: {4p, 4d, 5s, 5p}; H: {1s}; C, O: {ns, np}. At least 12n+m+8k bands are calculated in VASP for a Ru<sub>55</sub>H<sub>m</sub>X<sub>k</sub> compound. The charge spilling, a criterion that assesses the quality of the projection is systematically lower than 0.7%. Atomic charges are provided both by integrating the pDOS up to the Fermi energy. This is nothing else than a Mulliken population analysis done with an orthogonal basis set.

**DFT-NMR calculations.** As already pointed out above, Nuclear Magnetic Resonance (NMR) is a key spectroscopic method within the characterization of the surface composition of nanoparticles. In the past years, several studies carried out on NPs produced via organometallic synthetic route took advantage of this technique in order to determine the coordination mode and strength of different ancillary ligands (by <sup>13</sup>C or <sup>15</sup>N NMR),<sup>49</sup> or the presence of mobile surface hydrides at the NP surface (by solid-state <sup>2</sup>H NMR spectroscopy)<sup>68</sup>. Numerous studies demonstrate the accuracy of theoretical <sup>1</sup>H and <sup>13</sup>C NMR values using the gauge-invariant atomic orbital (GIAO)<sup>69,70</sup> for the calculation of the isotropic shielding and chemical shifts of organic compounds,<sup>71-74</sup> organometallic mononuclear metallic complexes,<sup>75,76</sup> or organometallic clusters.<sup>48,77</sup> Theoretical DFT-GIAO chemical shifts values are satisfactorily accurate with respect to experimental ones with an error often lower than 5% for <sup>1</sup>H and <sup>13</sup>C NMR shifts. Thus, theoretical calculations can be used as a complementary tool for exploring the structural properties of different systems in relationship with NMR experiments. However, despite the seminal work of Mauri and co-workers,<sup>78</sup> there is no general and easily available method for computing NMR shifts in metals, in the sense that both orbital and Knight shifts are computed. Yet, owing to the local nature of chemical shielding, we have often observed the transferability of chemical shifts calculated on small metal model clusters to those computed on NPs (the main idea behind this good correlation is that ligands adsorbed on specific sites on metal

NPs can be reproduced within smaller models such as molecular clusters).<sup>49-51</sup> This computational strategy has been adopted in the present work.

All NMR calculations were carried out using the *Gaussian09* software<sup>79</sup> on several [Ru<sub>4</sub>], [Ru<sub>5</sub>] and [Ru<sub>6</sub>] model ruthenium carbonyl clusters. For extra discussions on the accuracy of DFT<sup>13</sup>C-NMR calculations for carbon atoms enclosed in transition metal clusters, see Section 2a in the ESI. Concerning the charge and multiplicity of the [Ru<sub>4</sub>], [Ru<sub>5</sub>] and [Ru<sub>6</sub>] models employed in the present DFT-GIAO study, all these clusters are neutral/singlet species. In this way, the ruthenium carbonyl clusters can be seen as scale models that reproduce as close as possible some specific sites on the surface of diamagnetic RuNPs. Chemical shifts are calculated as  $\delta_{\text{iso}} = (\sigma_{\text{iso,ref}} - \sigma_{\text{iso,sample}})$  where  $\sigma_{\text{iso,ref}}$  is the isotropic chemical shielding of hydrogen or carbon atoms in tetramethylsilane (TMS). The calculated isotropic shielding for carbon in TMS is found to be 196.98 ppm at the DFT-PBE0<sup>80</sup> level of theory using the standard Pople's 6-31G(d,p) basis set. For the Ru atoms, the Stuttgart ECP pseudopotential<sup>81</sup> and its double-zeta quality basis set are employed, with an additional polarization function ( $\zeta_r$ : 1.235).

## Conflicts of interest

There are no conflicts to declare.

## Acknowledgements

The authors thank the HPC CALcul en Midi-Pyrénées (CALMIP-OLYMPE, grant P1415) for generous allocations of computer time. The computational resources provided by the high-performance computational facility of the Babeş-Bolyai University (MADECIP, POSCCE, COD SMIS 48801/1862) are also acknowledged. I.-T.M. thanks for financial support to a grant of the Romanian CNCS-UEFISCDI, project number PN-III-P4-ID-PCE-2016-0351, within PNCDI III. I.-T.M. also acknowledges the financial support received through the project: Entrepreneurship for innovation through doctoral and postdoctoral research, POCU/360/6/13/123886 co-financed by the European Social Fund, through the Operational Program for Human Capital 2014-2020. We additionally thank ERC Advanced Grant (MONACAT 2015-694159) for financial support.

## References

- R. B. Levy and M. Boudart, *Science*, 1973, **181**, 547.
- A. L. Stottlemyer, T. G. Kelly, Q. Meng and J. G. Chen, *Surf. Sci. Rep.*, 2012, **67**, 201.
- H. Hwu and J. G. Chen, *Chem. Rev.*, 2005, **105**, 185.
- A. Nandula, Q. T. Trinh, M. Saeys and A. N. Alexandrova, *Angew. Chem. Int. Ed.*, 2015, **54**, 5312.
- Y.-Y. Ma, Z.-L. Lang, L.-K. Yan, Y.-H. Wang, H.-Q. Tan, K. Feng, Y.-J. Xia, J. Zhong, Y. Liu, Z.-H. Kang and Y.-G. Li, *Energy Environ. Sci.*, 2018, **11**, 2114.
- C. G. Morales-Guio, L.-A. Stern and X. Hu, *Chem. Soc. Rev.*, 2014, **43**, 6555.
- Y. Ma, G. Guan, X. Hao, J. Cao and A. Abudula, *Renew. Sust. Energ. Rev.*, 2017, **75**, 1101.
- J. Yang, Y. Xie, R. Wang, B. Jiang, C. Tian, G. Mu, J. Yin, B. Wang and H. Fu, *ACS Appl. Mater. Interfaces*, 2013, **5**, 6571.
- N. Ji, T. Zhang, M. Zheng, A. Wang, H. Wang, X. Wang and J. G. Chen, *Angew. Chem. Int. Ed.*, 2008, **47**, 8510.
- W. Chen, T. Lin, Y. Dai, Y. An, F. Yu, L. Zhong, S. Li and Y. Sun, *Catal. Today*, 2018, **311**, 8.
- H. Schulz, *Appl. Catal. A*, 1999, **186**, 3.
- E. van Steen and M. Claeys, *Chem. Eng. Technol.*, 2008, **31**, 655.
- C. I. Méndez and J. Ancheyta, *Catal. Today*, 2020, **353**, 3.
- E. de Smit and B. M. Weckhuysen, *Chem. Soc. Rev.*, 2008, **37**, 2758.
- K. Xu, B. Sun, J. Lin, W. Wen, Y. Pei, S. Yan, M. Qiao, X. Zhang and B. Zong, *Nat. Commun.*, 2014, **5**, 5783.
- T. A. Wezendonk, X. Sun, A. I. Dugulan, A. J. F. van Hoof, E. J. M. Hensen, F. Kapteijn and J. Gascon, *J. Catal.*, 2018, **362**, 106.
- R. J. P. Broos, B. Zijlstra, I. A. W. Filot and E. J. M. Hensen, *J. Phys. Chem. C*, 2018, **122**, 9929.
- A. Y. Khodakov, W. Chu and P. Fongarland, *Chem. Rev.*, 2007, **107**, 1692.
- J. X. Liu, H. Y. Su, D. P. Sun, B. Y. Zhang and W. X. Li, *J. Am. Chem. Soc.*, 2013, **135**, 16284.
- B. Zijlstra, R. J. P. Broos, W. Chen, G. L. Bezemer, I. A. W. Filot and E. J. M. Hensen, *ACS Catal.*, 2020, **10**, 9376.
- R. Zhang, L. Kang, H. Liu, B. Wang, D. Li and M. Fan, *Appl. Catal. B: Environ.*, 2020, **269**, 118847.
- X.-Y. Quek, I. A. W. Filot, R. Pestman, R. A. van Santen, V. Petkov and E. J. M. Hensen, *Chem. Commun.*, 2014, **50**, 6005.
- J. M. González-Carballo, F. J. Pérez-Alonso, M. Ojeda, F. J. García-García, J. L. G. Fierro and S. Rojas, *ChemCatChem*, 2014, **6**, 2084.
- J. Kang, S. Zhang, Q. Zhang and Y. Wang, *Angew. Chem., Int. Ed.*, 2009, **48**, 2565.
- I. A. W. Filot, R. A. van Santen and E. J. M. Hensen, *Catal. Sci. Technol.*, 2014, **4**, 3129.
- M. A. Petersen, J. A. van den Berg and W. J. van Rensburg, *J. Phys. Chem. C*, 2010, **114**, 7863.
- Y. P. Pei, J. X. Liu, Y. H. Zhao, Y. J. Ding, T. Liu, W. D. Dong, H. J. Zhu, H. Y. Su, L. Yan, J. L. Li and W. X. Li, *ACS Catal.*, 2015, **5**, 3620.
- M. R. Axet and K. Philippot, *Chem. Rev.*, 2020, **120**, 1085.
- F. Anya and D. Resasco, *ACS Catal.*, 2020, **10**, 4433.
- L. Foppa, C. Copéret and A. Comas-Vives, *J. Am. Chem. Soc.*, 2016, **138**, 16655.
- L. Foppa, M. Iannuzzi, C. Copéret and A. Comas-Vives, *ACS Catal.*, 2018, **8**, 6983.
- L. Foppa, M. Iannuzzi, C. Copéret and A. Comas-Vives, *ACS Catal.*, 2019, **9**, 6571.
- S. Shetty, A. P. J. Jansen and R. A. van Santen, *J. Am. Chem. Soc.*, 2009, **131**, 12874.
- S. Shetty and R. A. van Santen, *Catal. Today*, 2011, **171**, 168.
- P. Zhao, Y. He, D.-B. Cao, H. Xiang, H. Jiao, Y. Yang, Y.-W. Li and X.-D. Wen, *J. Phys. Chem. C*, 2019, **123**, 6508.
- I. M. Ciobica and R. A. van Santen, *J. Phys. Chem. B*, 2003, **107**, 3808.
- L. Cusinato, L. M. Martínez-Prieto, B. Chaudret, I. del Rosal and R. Poteau, *Nanoscale*, 2016, **8**, 10974.
- B. T. Loveless, C. Buda, M. Neurock and E. Iglesia, *J. Am. Chem. Soc.*, 2013, **135**, 6107.
- D. Hibbitts, B. T. Loveless, M. Neurock and E. Iglesia, *Angew. Chem. Int. Ed.*, 2013, **52**, 12273.
- J. Liu, D. Hibbitts and E. Iglesia, *J. Am. Chem. Soc.*, 2017, **139**, 11789.
- D. Hibbitts and E. Iglesia, *Acc. Chem. Res.*, 2015, **48**, 1254.
- S. Takemoto and H. Matsuzaka, *Coord. Chem. Rev.*, 2012, **256**, 574.
- T. M. Duncan, P. Winslow and A. T. Bell, *Chem. Phys. Lett.*, 1983, **102**, 163.



- 44 T. M. Duncan, P. Winslow and A. T. Bell, *J. Catal.*, 1985, **93**, 1.
- 45 J. García-Antón, M. R. Axet, S. Jansat, K. Philippot, B. Chaudret, T. Pery, G. Buntkowsky and H.H. Limbach, *Angew. Chem. Int. Ed.*, 2008, **47**, 2074.
- 46 L. M. Martínez-Prieto, S. Carenco, C. H. Wu, E. Bonnefille, S. Axnanda, Z. Liu, P. F. Fazzini, K. Philippot, M. Salmeron and B. Chaudret, *ACS Catalysis*, 2014, **4**, 3160.
- 47 C. M. T. Hayward, J. R. Shapley, M. R. Churchill, C. Bueno and A. L. Rheingold, *J. Am. Chem. Soc.*, 1982, **104**, 7347.
- 48 I. del Rosal, F. Jolibois, L. Maron, K. Philippot, B. Chaudret and R. Poteau, *Dalton Trans.*, 2009, 2142.
- 49 L. M. Martínez-Prieto, I. Cano, A. Márquez, E. A. Baquero, S. Tricard, L. Cusinato, I. del Rosal, R. Poteau, Y. Coppel, K. Philippot, B. Chaudret, J. Cámpora and P. W. N. M. van Leeuwen, *Chem. Sci.*, 2017, **8**, 2931.
- 50 R. González-Gómez, L. Cusinato, C. Bijani, Y. Coppel, P. Lecante, C. Amiens, I. del Rosal, K. Philippot and R. Poteau, *Nanoscale*, 2019, **11**, 9392.
- 51 E. Martin Morales, Y. Coppel, P. Lecante, I. del Rosal, R. Poteau, J. Esvan, P. Sutra, K. Philippot and A. Igau, *Chem. Commun.*, 2020, **56**, 4059.
- 52 L. Foppa, K. Yamamoto, W.-C. Liao, A. Comas-Vives and C. Copéret, *J. Phys. Chem. Lett.*, 2018, **9**, 3348.
- 53 C. Pan, K. Pelzer, K. Philippot, B. Chaudret, F. Dassenoy, P. Lecante and M. J. Casanove, *J. Am. Chem. Soc.*, 2001, **123**, 7584.
- 54 G. Kresse and J. Fürthmüller, *Phys. Rev. B*, 1996, **54**, 11169.
- 55 G. Kresse and J. Fürthmüller, *Comput. Mater. Sci.*, 1996, **6**, 15.
- 56 J. P. Perdew, K. Burke and M. Ernzerhof, *Phys. Rev. Lett.*, 1996, **77**, 3865.
- 57 P. E. B. Blöchl, *Phys. Rev. B*, 1994, **50**, 17953.
- 58 G. Kresse and D. Joubert, *Phys. Rev. B*, 1999, **59**, 1758.
- 59 I. del Rosal, L. Truflandier, R. Poteau and I. C. Gerber, *J. Phys. Chem. C*, 2011, **115**, 2169.
- 60 I. Del Rosal, M. Mercy, I. C. Gerber and R. Poteau, *ACS Nano*, 2013, **7**, 9823.
- 61 H. J. Monkhorst and J. D. Pack, *Phys. Rev. B*, 1976, **13**, 5188.
- 62 G. Henkelman, B. P. Uberuaga and H. Jonsson, *J. Chem. Phys.*, 2000, **113**, 9901.
- 63 G. Henkelman and H. Jonsson, *J. Chem. Phys.*, 2000, **113**, 9978.
- 64 D. Sheppard, R. Terrell and G. Henkelman, *J. Chem. Phys.*, 2008, **128**, 134106.
- 65 V. L. Deringer, A. L. Tchougréeff and R. Dronskowski, *J. Phys. Chem. A*, 2011, **115**, 5461.
- 66 S. Maintz, V. L. Deringer, A. L. Tchougréeff and R. Dronskowski, *J. Comput. Chem.*, 2013, **34**, 2557.
- 67 S. Maintz, V. L. Deringer, A. L. Tchougréeff, and R. Dronskowski, *J. Comput. Chem.*, 2016, **37**, 1030.
- 68 T. Pery, K. Pelzer, G. Buntkowsky, K. Philippot, H. H. Limbach and B. Chaudret, *ChemPhysChem*, 2005, **6**, 605.
- 69 K. Wolinski, J. F. Hinton and P. Pulay, *J. Am. Chem. Soc.*, 1990, **112**, 8251.
- 70 J. R. Cheeseman, G. W. Trucks, T. A. Keith and M. J. Frisch, *J. Chem. Phys.*, 1996, **104**, 5497.
- 71 D. A. Forsyth and A. B. Seabag, *J. Am. Chem. Soc.*, 1997, **119**, 9483.
- 72 A. Wu, Y. Zhang, X. Xu and Y. Yan, *J. Comput. Chem.*, 2007, **28**, 2431.
- 73 T. Helgaker, M. Jaszuński and K. Ruud, *Chem. Rev.*, 1999, **99**, 29.
- 74 K. Dybiec and A. Gryff-Keller, *Magn. Reson. Chem.*, 2009, **47**, 63.
- 75 I. del Rosal, L. Maron, R. Poteau and F. Jolibois, *Dalton Trans.*, 2008, 3959.
- 76 N. Popoff, J. Espinas, J. Pelletier, B. Macqueron, K. C. Szeto, O. Boyron, C. Boisson, I. del Rosal, L. Maron, A. De Mallmann, R. M. Gauvin and M. Taoufik, *Chem. Eur. J.*, 2013, **19**, 964.
- 77 B. Le Guennic, J. Neugebauer, M. Reiher and J. Autschbach, *Chem. Eur. J.*, 2005, **11**, 1677.
- 78 M. d'Avezac, N. Marzari and F. Mauri, *Phys. Rev. B*, 2007, **76**, 165122.
- 79 M. J. Frisch, G. W. Trucks, H. B. Schlegel, G. E. Scuseria, M. A. Robb, J. R. Cheeseman, G. Scalmani, V. Barone, B. Mennucci, G. A. Petersson, H. Nakatsuji, M. Caricato, X. Li, H. P. Hratchian, A. F. Izmaylov, J. Bloino, G. Zheng, J. L. Sonnenberg, M. Hada, M. Ehara, K. Toyota, R. Fukuda, J. Hasegawa, M. Ishida, T. Nakajima, Y. Honda, O. Kitao, H. Nakai, T. Vreven, J. A. Montgomery, Jr., J. E. Peralta, F. Ogliaro, M. Bearpark, J. J. Heyd, E. Brothers, K. N. Kudin, V. N. Staroverov, R. Kobayashi, J. Normand, K. Raghavachari, A. Rendell, J. C. Burant, S. S. Iyengar, J. Tomasi, M. Cossi, N. Rega, J. M. Millam, M. Klene, J. E. Knox, J. B. Cross, V. Bakken, C. Adamo, J. Jaramillo, R. Gomperts, R. E. Stratmann, O. Yazyev, A. J. Austin, R. Cammi, C. Pomelli, J. W. Ochterski, R. L. Martin, K. Morokuma, V. G. Zakrzewski, G. A. Voth, P. Salvador, J. J. Dannenberg, S. Dapprich, A. D. Daniels, O. Farkas, J. B. Foresman, J. V. Ortiz, J. Cioslowski and D. J. Fox, *Gaussian 09 Revision D.01*, Gaussian Inc. Wallingford CT 2009.
- 80 C. Adamo and V. Barone, *J. Chem. Phys.*, 1999, **110**, 6158.
- 81 M. Dolg, U. Wedig, H. Stoll and H. Preuss, *J. Chem. Phys.*, 1987, **86**, 866.